

# ACF-Net: An Attention-enhanced Co-interactive Fusion Network for Automated Structural Condition Assessment in Visual Inspection

Chenyu Zhang<sup>a</sup>, Zhaozheng Yin<sup>b</sup>, Ruwen Qin<sup>a</sup>

<sup>a</sup>*Department of Civil Engineering, Stony Brook University, 2427 Computer Science, Stony Brook, 11794, New York, United States*

<sup>b</sup>*Department of Computer Science, Department of Biomedical Informatics, and AI Institute, Stony Brook University, 2313B Computer Science Building, Stony Brook, 11794, New York, United States*

---

## Abstract

Efficiently monitoring the condition of civil infrastructures necessitates automating the structural condition assessment in visual inspection. This paper proposes an Attention-enhanced Co-interactive Fusion Network (ACF-Net) for automatic structural condition assessment in visual bridge inspection. The ACF-Net can simultaneously parse structural elements and segment surface defects on the elements in inspection images. It integrates two task-specific relearning subnets to extract task-specific features from an overall feature embedding and a co-interactive feature fusion module to capture the spatial correlation and facilitate information sharing between tasks. Experimental results demonstrate that the proposed ACF-Net outperforms the current state-of-the-art approaches, achieving promising performance with 92.11% mIoU for element parsing and 87.16% mIoU for corrosion segmentation on the new benchmark dataset Steel Bridge Condition Inspection Visual (SBCIV) testing set. An ablation study reveals the strengths of ACF-Net, and a case study showcases its capability to automate structural condition assessment. The code will be open-source after acceptance.

*Keywords:* Infrastructure inspection, Multitask learning, Co-interactive fusion, Structural element parsing, Defect segmentation

*PACS:* 0000, 1111

*2000 MSC:* 0000, 1111

---

## 1. Introduction

Visual inspection, a crucial component of structural health monitoring (SHM), is performed periodically to evaluate the condition of infrastructure [1]. However, traditional manual inspections have inherent limitations. Desires for time-cost efficiency, reliability, and safety have driven a growing interest in automating visual inspection with cutting-edge technologies like robotics and artificial intelligence [2]. Unmanned aerial vehicles (UAVs), equipped with one or multiple types of non-destructive evaluation sensors, have gained popularity for capturing inspection videos and images of infrastructure [3]. Maximizing the potential of robotic inspection platforms and the automation process necessitates the employment of efficient and reliable techniques for inspection image analysis. Deep convolutional neural networks (DCNNs), in particular, have shown tremendous potential for analyzing images and extracting vital information about the inspected structures, inspiring researchers to investigate their applications in SHM [4]. For example, a drone with mounted RGB cameras can quickly assess the condition of a bridge at the inspection site and narrow down to spots where other high-resolution yet time-consuming diagnostic sensors should be used to collect detailed information, such as infrared sensors, ground-penetrating radar, ultrasound scanning, and others.

According to the infrastructure inspection manuals and standards [5, 6, 7, 8], it is necessary to associate structural elements with the severity of defects developed in the elements to evaluate the condition of individual elements, which builds the foundation for assessing the condition of the overall structure. That is, it is required to not only recognize and localize key structural elements and defects in the inspection images captured by inspection robots, but also spatially associate them. This capability will offer a reference for prioritizing subsequent structural condition assessment that is usually more expensive.

Researchers have made progress in identifying or segmenting structural elements and defects using DCNNs [9, 10, 11]. However, most studies were dedicated to addressing one task, leading to three challenges in deep learning-based visual inspection. Firstly, the appearance of structural elements may be inaccurately recognized due to the presence of surface defects. For example, Fig. 1(a) shows a rusted girder section and a below-bearing share similar surface defects. The girder's rusted or flaking portion might be mistakenly identified as part of the bearing due to the similarities in appearance caused

by the defects. Secondly, surface inhomogeneity, shadows, and poor lighting conditions, as shown in Fig. 1(b), continue to pose challenges for reliably assessing defects on surfaces of structural elements. Lastly, the spatial correlation between element parsing and defect segmentation tasks, as shown in Fig. 1(c), has been overlooked, leading to unreasonable predictions. For example, the presence of steel corrosion in the background area is apparently a wrong prediction result because it is impossible in reality. Several attempts have explored solutions to these challenges, mainly using multi-task learning (MTL) methods [12, 13, 14]. MTL presents an efficient approach that learns to perform the two related tasks simultaneously with a unified model [15]. While those studies have laid a solid foundation for visual assessment of the structure’s condition, several research needs must be addressed further to improve the technology readiness of image analysis for automated visual inspection.

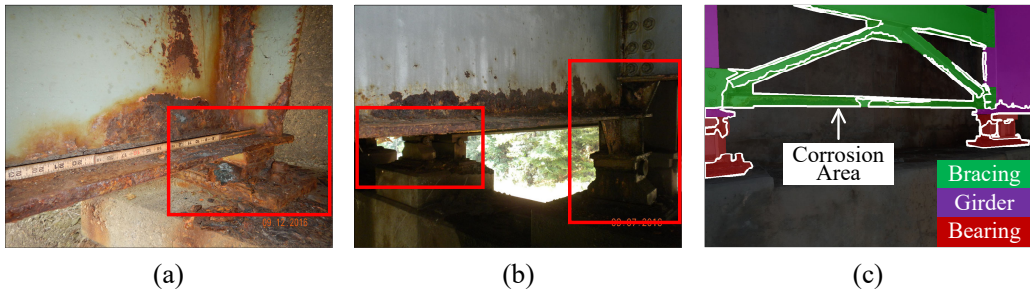


Figure 1: Challenges in deep learning-based visual inspection (Base images courtesy of [16]).

MTL can adopt a powerful deep encoder that extracts a deep feature embedding to represent each input inspection image [15]. There are many choices of deep encoders for semantic segmentation. The guidance for choosing one deep encoder that is well-suited for the tasks of this paper has not been available. Moreover, the overall embedding encompasses information related to both structural elements and surface defects. While a simple method named feature projection [14] has been developed to attempt to decouple task-specific features intertwined in the overall embedding, feature relearning has not been explored, which is a more advanced method to extract task-specific features. Last but not least, how to leverage the spatial correlation between structural elements and defects to let one task benefit from the other task and vice versa is still an unsolved question. A cross-

talk method [14] was created for this purpose. However, that design does not explicitly integrates the physical meaning of spatial information that one task can provide to another. The spatial attention mechanism, which focuses on spatial attributes such as shape and boundaries within an image, is critical in image analysis. Upon obtaining the spatial attention maps and task-specific features, the design of a suitable network architecture becomes pivotal. Such an architecture should facilitate efficient communication and information exchange with these attention and feature maps across varying tasks. Incorporating this diverse information can enhance a model’s understanding of the complex interrelations within the data, leading to more robust feature representations and improved semantic segmentation outcomes.

In addressing the above-discussed technical needs, this paper has the following contributions:

- A new Attention-enhanced Co-interactive Fusion MTL model, named ACF-Net, is introduced. It has a share-split-interaction pipeline composed of a shared high-resolution deep encoder, two task-specific re-learning subnets, and a co-interactive feature fusion module.
- A new dataset, named Steel Bridge Condition Inspection Visual (SB-CIV) dataset, is developed to support the development and evaluation of MTL models for automating the bridge element inspection.
- A comprehensive study employing both numerical experiments and qualitative results is conducted to verify the strengths of ACF-Net and reveal reasons for achieving satisfying performance.

Based on the proposed ACF-Net, the automatic structural condition assessment framework in visual bridge inspection is shown in Fig. 2.

The remainder of the paper is organized as follows. The next section is a summary of related work. Then, Section 3 presents the architecture design of ACF-Net, followed by the details of executing the model. Section 5 discusses results from the experimental studies for evaluating ACF-Net, and Section 6 further presents the assessment case study. In the end, Section 7 summarizes insights gained from this study and suggestions for important future work.

## 2. Related work

This paper is built on studies that contribute to structural condition assessment in visual inspection, either directly or indirectly. The related

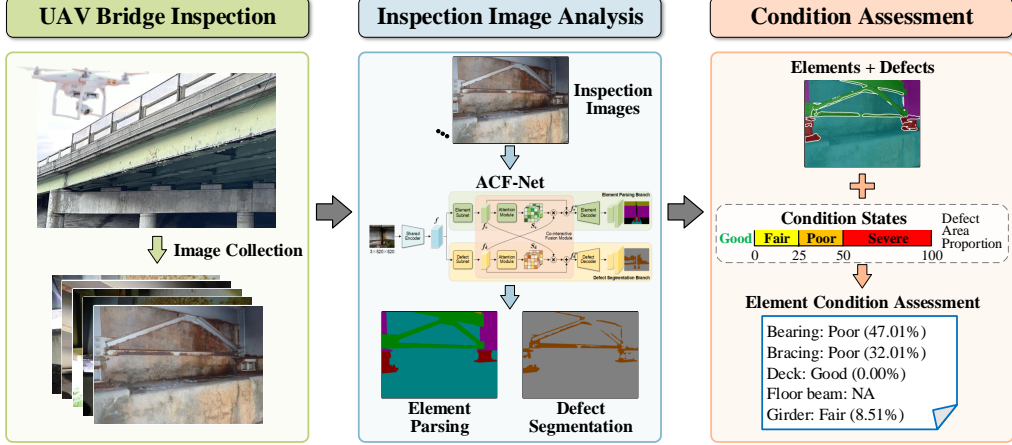


Figure 2: Framework of the automated structural condition assessment in visual bridge inspection based on ACF-Net (Example images courtesy of Shengqian Zheng and [16]).

literature is summarized below.

### 2.1. DCNN-based defect segmentation

An intensively studied topic related to the visual inspection of infrastructures is defect detection, which is about finding structural surface defects or damage in inspection images or videos [17]. The majority of current research efforts are centered on DCNN-based **defect segmentation**, where each pixel of an inspection image is classified as defect or non-defect [18]. Segmentation can provide pixel-level position information of defects, resulting in superior accuracy compared to object detection methods [19]. Deep feature extractors, such as DCNNs, are employed due to their ability to facilitate automated representation learning and embed rich information, ultimately capturing complex real-world data features through multi-level feature abstraction [20].

DCNN-based crack segmentation methods have shown considerable success in detecting and analyzing defects across various civil structures, including buildings, bridges, tunnels, and roads [21]. Dung and Anh [22] utilized a Fully Convolutional Network (FCN) [23] for crack element marking, while Ji et al. [24] aimed at accurately quantifying cracks by training an atrous convolution-based DeepLabv3+ model [25]. Mei et al. [26] focused on crack connectivity through a densely connected DCNN architecture. Liu and Wang [27] incorporated visual explanations into a U-Net [28] based model to high-

light crack semantics.

Recently, DCNNs have been utilized for the detection and segmentation of corrosion in steel structures. Atha and Jahanshahi [29] demonstrated that DCNNs surpass conventional vision-based corrosion detection methods that rely on texture and color analysis using a basic multilayer perceptron network. Rahman et al. [30] introduced a corrosion assessment approach that applied DeepLab [31] to infrastructure inspection images. Han et al. [32] developed a two-stage corrosion location method by integrating Feature Pyramid Network (FPN) [33] and Path Aggregation Network (PANet) [34] to identify corrosion areas on structural surfaces. Jiang et al. [35] proposed an enhanced U-net, Fusion-Attention-U-net (FAU-net), which incorporated a fusion module and an attention module within the U-net for segmenting three types of corrosion-related damage within dim steel box girders. Katsamenis et al. [36] applied U-Net for the automated simultaneous detection and localization of corrosion and rust grade recognition from inspection images of metal structures. These studies have laid a solid methodological groundwork for identifying defects in structural elements.

## 2.2. DCNN-based structural element parsing

Structural element inspection requires associating elements with defects developed on them. A stream of recent studies was motivated to focus on ***structural element parsing*** in inspection images using various DCNN-based methods. This parsing process aims at identifying structural elements within these images, typically achieved through object detection or segmentation within the given scene. Accurate identification of critical elements enables a thorough and precise evaluation of the infrastructure's overall condition, considering factors like defect shape, size, location, and compliance with established standards. Gao and Mosalam [37] developed a hierarchical framework applicable to a range of classification tasks, including recognizing building component types of damage states. Yeum et al. [38] detected damage in welded joints on truss structures by extracting and classifying target image areas. Narazaki et al. [9] presented an FCN-based method for bridge component recognition. Czerniawski and Leite [39] developed a DeepLab-based model incorporating RGB-D (color and depth) images for component segmentation in thirteen buildings. Wang et al. [40] proposed an enhanced U-Net model with a novel geometric consistency loss for geometry-informed structural component segmentation of post-earthquake buildings. Karim et al. [10] transferred a pre-trained Mask R-CNN [41] to the task

of bridge elements segmentation and created a semi-supervised self-training method to refine the transferred network iteratively. Through a comparative analysis of the state-of-the-art semantic segmentation networks, Zhang et al. [42] revealed the aptitude of High-Resolution Network (HRNet) [43] in efficiently extracting deep features for segmenting various structural elements in bridge inspection images. Furthermore, the study investigated factors that impact the network’s performance, such as transfer learning, the size of the training set, data augmentation techniques, and the role of class weights.

Although impressive, the above methods exhibit some limitations in identifying and capturing the highly irregular and significantly deteriorated elements from inspection images. Furthermore, these approaches have yet to explore feature fusion’s potential to enhance element parsing capability. Notably, compared to the extensively studied defect segmentation, structural element parsing remains in a relatively nascent stage of development.

### *2.3. MTL in visual structural assessment*

MTL has proven effective in various civil engineering applications, such as SHM data reconstruction [44], bridge damage diagnosis [45], landslide evolution state prediction [46], and more. The prevalent method for achieving MTL is to share the feature extractor and branch downstream tasks for respective predictions [47]. This shared feature extractor learns common representations for all tasks, significantly reducing the risk of overfitting and enhancing generalization [15]. However, one task can easily dominate others in this conventional approach, which negatively impacts the overall performance.

Hoskere et al. [12] introduced MaDnet, a DCNN comprising a shared feature extractor and multiple semantic segmentation pathways to identify material and damage types. This framework indicates that one segmentation task can provide contextual information for another. Ye et al. [13] developed MT-HRNet that employs the HRNetV2-W18 backbone and two segmentation heads for element recognition and damage identification in synthetic bridge images. To further address the challenges of task domination and improve task-specific feature sharing, Zhang et al. [14] proposed MTL-D and MTL-I models that both can simultaneously segment bridge elements and surface corrosion. These models project the shared features for respective tasks and utilize the cross-talk feature sharing between tasks to enhance performance and prevent the dominance of a single task.

Despite remarkable advancements in this direction, most studies remain at the stage of naïve MTL models. While attempts were observed to exchange information among different tasks, they have yet to explicitly model the spatial association between elements and defects. The effective utilization of this spatial relationship will mitigate the task domination issue and enhance the overall performance, which remains a further exploration.

### 3. ACF-Net

In filling the above-discussed gaps, this paper introduces an Attention-enhanced Co-interactive Fusion Network (ACF-Net), shown in Fig. 3. ACF-Net analyzes each input RGB inspection image to parse the bridge in the images into structural elements and segment the surface defects on the elements. The backbone of ACF-Net encodes the input image as an overall feature embedding. Then, two relearning subnets respectively extract element- and defect-specific feature maps from the encoded overall embedding. After that, a co-interactive module generates spatial attention maps to guide the feature fusion for performing the two downstream tasks. Finally, two reconstruction decoders respectively perform the pixel-level classification for element parsing and defect segmentation. Details of the ACF-Net’s key components are delineated below.

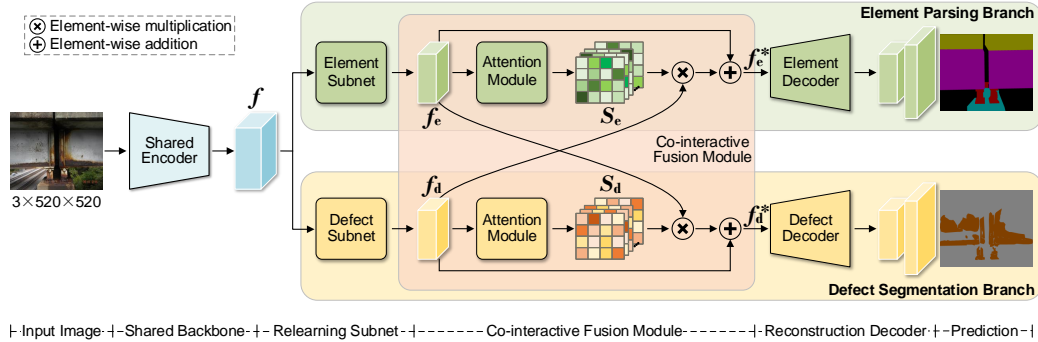


Figure 3: Architecture of the ACF-Net.

#### 3.1. Shared encoder

ACF-Net chooses HRNetV2-W48 [43] as its shared encoder, which generates high-resolution representations through the parallel connection of high-

to-low-resolution convolutions. An inspection image captured by the robot-mounted RGB camera is reshaped to be the size  $3 \times 520 \times 520$  before entering the encoder. The shared encoder extracts an overall feature embedding,  $\mathbf{f} (\in \mathbb{R}^{720 \times 120 \times 120})$ , from the input image, which encompasses both the bridge element and defect information in the image.

### 3.2. Task-specific feature relearning subnets

Let  $\Omega = \{e, d\}$  denote the index set of tasks, where  $e$  and  $d$  are the indices of element parsing and defect segmentation tasks, respectively. These two tasks concentrate on distinct characteristics and minutiae. Therefore, following the shared encoder are two task-specific relearning subnets that further extract the task-specific feature maps,  $\mathbf{f}_i (\in \mathbb{R}^{512 \times 120 \times 120})$ , for  $i \in \Omega$ . Each relearning subnet consists of a convolutional layer (COV), a batch normalization layer (BN), and the rectified linear unit (ReLU) activation function in sequence:

$$\mathbf{f}_i = \text{ReLU}(\text{BN}(\text{COV}(\mathbf{f}; \boldsymbol{\theta}_{\text{rln},i}))), \forall i \in \Omega \quad (1)$$

The convolutional operation in Eq. (1) uses a kernel size of 3, a stride of 1, padding of 1, and 512 output channels.  $\boldsymbol{\theta}_{\text{rln},i}$  are learnable parameters of the convolutional layer in the relearning (rln) subnet for task  $i$ .

### 3.3. Co-interactive fusion module

Structural elements and defects exhibit spatial correlation. Therefore, exchanging information between the two tasks can positively impact their performance, which motivates the design of the co-interactive fusion module. The task-specific feature map of one task is fused with the additional spatial information from the other task in an additive manner:

$$\mathbf{f}_i^* = \mathbf{f}_i \oplus (\mathbf{S}_i \otimes \mathbf{f}_j), \forall i, j \in \Omega \text{ and } i \neq j \quad (2)$$

Here,  $\otimes$  represents the element-wise multiplication,  $\oplus$  denotes the element-wise addition,  $\mathbf{S}_i (\in \mathbb{R}^{512 \times 120 \times 120})$  is the spatial attention mask for guiding the feature fusion for task  $i$ , and  $\mathbf{f}_i^*$  is the resulting spatial-attention-enhanced feature map for the task.

In Eq. (2), the spatial attention mask of one task consists of scores for adjusting the other task's feature map in feature fusion. These scores are

learned by a convolutional layer (with a kernel size of 3, a stride of 1, and padding of 1) and normalized using the Sigmoid function:

$$\mathbf{S}_i = \text{Sigmoid}(\text{COV}(\mathbf{f}_i; \boldsymbol{\theta}_{\text{att},i})), \forall i \in \Omega \quad (3)$$

where  $\boldsymbol{\theta}_{\text{att},i}$  are the learnable parameters of the attention (att) module for task  $i$ .

### 3.4. Reconstruction decoder

In leaving the co-interactive fusion module, the spatial-attention-enhanced feature map for any task  $i$ ,  $\mathbf{f}_i^*$ , flows into the task's reconstruction decoder. First, the segmentation head (SH) in the decoder performs the pixel-level classification, which is composed of a convolutional layer (with a kernel size of 1, a stride of 1, and 512 output channels), a batch normalization layer, a ReLU activation function, and another convolutional layer (with a kernel size of 1, a stride of 1, and  $N_i$  output channels). Then, the obtained segmentation map is upsampled (UP) using the bilinear interpolation to give the pixel-level prediction scores for all classes,  $\hat{\mathbf{y}}_i$  ( $\in \mathbb{R}^{N_i \times 520 \times 520}$ ). That is,

$$\hat{\mathbf{y}}_i = \text{UP}(\text{SH}(\mathbf{f}_i^*; \boldsymbol{\theta}_{\text{sh},i})), \forall i \in \Omega \quad (4)$$

where  $\boldsymbol{\theta}_{\text{sh},i}$  are learnable parameters of the convolutional layers in the segmentation head of task  $i$ .

### 3.5. Loss function

Learnable parameters of the proposed ACF-Net are determined through model training that minimizes a differentiable loss function through back-propagation. The loss function is an aggregated measure of the pixel-level dissimilarity between the ground truth and prediction on a training dataset.

Images in the training dataset are indexed by  $k$ ,  $\mathbf{y}_i(k)$  ( $\in \mathbb{R}^{N_i \times 520 \times 520}$ ) represents the one-hot encoding of the image's pixel-level ground truth associated with task  $i$ , and  $\hat{\mathbf{y}}_i(k)$  ( $\in \mathbb{R}^{N_i \times 520 \times 520}$ ) denotes the pixel-level prediction. The cross-entropy loss of ACF-Net in performing task  $i$  is

$$\mathcal{L}_i = - \sum_k \langle \mathbf{y}_i(k), \log \hat{\mathbf{y}}_i(k) \rangle, \forall i \in \Omega \quad (5)$$

where  $\langle \cdot, \cdot \rangle$  is the operation to obtain the Frobenius inner product on two tensors, which performs the element-wise product of the two input tensors

to become one in the same size and then sums up all the elements of the resulting tensor.

The loss functions defined for the individual tasks need to be integrated as a total loss function so that ACF-Net learns the two tasks at once. This paper employs a straightforward yet efficient weighting scheme, known as Dynamic Weight Average (DWA) [48], to adaptively balance the individual loss functions during training. Given that  $t$  is the index of training epochs and  $\mathcal{L}_{i,t}$  is the loss function of task  $i$  calculated using Eq. (5) at epoch  $t$ , the relative loss descending rates of the two tasks in the last training epoch are:

$$\mathbf{w}_{t-1} = \left[ \frac{\mathcal{L}_{e,t-1}}{\mathcal{L}_{e,t-2}}, \frac{\mathcal{L}_{d,t-1}}{\mathcal{L}_{d,t-2}} \right] \quad (6)$$

These rates are references for assigning weights to the individual loss functions at the current epoch.  $\mathbf{w}_t$  is initialized as  $[1, 1]$  at  $t = 1, 2$ . The weights  $\lambda_{e,t}$  and  $\lambda_{d,t}$  for aggregating the individual loss functions are obtained by applying the softmax operation to  $\mathbf{w}_{t-1}$ ,

$$\boldsymbol{\lambda}_t = 2 \times \text{Softmax}[\mathbf{w}_{t-1}/\tau] \quad (7)$$

where  $\boldsymbol{\lambda}_t = [\lambda_{e,t}, \lambda_{d,t}]$  is the vector of weights at  $t$ , and  $\tau$  is a temperature parameter for controlling the softness of this weighting scheme, chosen as 2 in this study.

The total loss function,  $\mathcal{L}_{\text{tot}}$ , is attained by aggregating the individual training loss functions  $\mathcal{L}_{e,t}$  and  $\mathcal{L}_{d,t}$  using the weights calculated in Eq. (7):

$$\mathcal{L}_{\text{tot}} = \lambda_{e,t} \mathcal{L}_{e,t} + \lambda_{d,t} \mathcal{L}_{d,t} \quad (8)$$

With the DWA scheme, a higher weight is put on the task with a smaller relative loss descending rate from the last training epoch.

## 4. Experimental setup

### 4.1. Dataset and data augmentation

Lacking publicly available datasets with the annotation for developing the proposed MTL model, this study created a new annotated dataset, the Steel Bridge Condition Inspection Visual (SBCIV) dataset, comprising 440 high-resolution images procured from two publicly available datasets: Corrosion Condition State Semantic Segmentation Dataset [49] and Common Objects

in Context for bridge inspection (COCO-Bridge) dataset [16]. 100 images are reserved for testing and evaluating the ACF-Net, and the remaining 340 images, split into the training dataset and validation dataset at the 9:1 ratio, are used for model development and hyperparameters optimization.

The SBCIV dataset provides the pixel-level annotation for six types of common structural elements of steel plate girder bridges, shown in Fig. 4, including bearing, bracing, deck, floor beam, girder, and substructure. Fig. 5 shows that the number of element types in an inspection image, as well as the number of bridge elements presented in an image, varies from one image to another. The dataset also provides the pixel-level binary annotation of surface defects: corrosion or non-corrosion. The annotations were developed using the LabelMe [50] labeling tool and adhered to the Bridge Inspector’s Reference Manual [7] and the corrosion condition state guidelines outlined in the American Association of State Highway and Transportation Officials (AASHTO) [6].

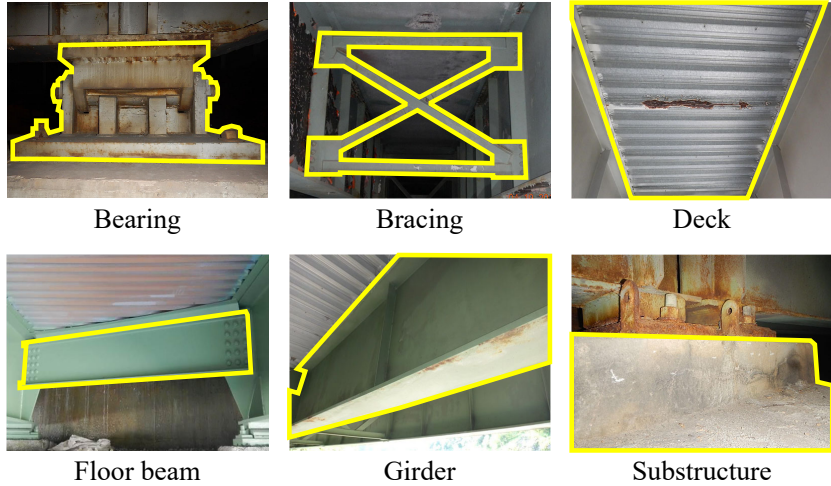


Figure 4: Illustration of bridge element classes (Base images courtesy of [16] and [49]).

Deep learning models usually require a large amount of data to be trained effectively. Yet, creating a large dataset with the required annotation for the problem of study is expensive. The issue of small data can be partially addressed by data augmentation that aims to not only increase the quantity of data but also cover as many situations as possible which were not in the original dataset but could occur in real-world scenarios. To achieve this, seven image data augmentation methods were employed in this paper, including

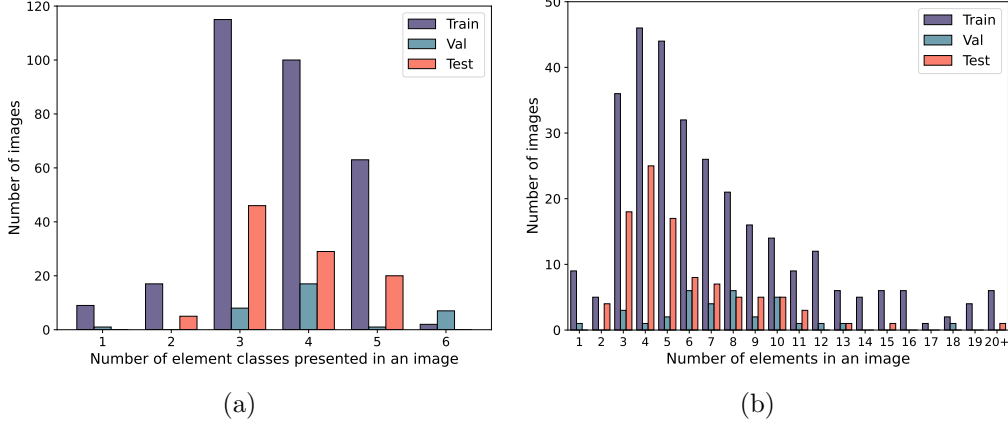


Figure 5: Distribution of SBCIV dataset: (a) by the number of element classes in an image, (b) by the number of elements in an image.

random scale transformation, random rotations between  $\pm 10^\circ$ , random horizontal flipping, random image intensity noise using  $5 \times 5$  Gaussian kernel, and HSV augment that randomly adjusts hue (H), saturation (S), and value (V) of images.

#### 4.2. Implementation details

The ACF-Net was built based on the PyTorch 1.10.0 library and trained on a server with an Nvidia Tesla V100 GPU (32 GB memory). The Adam optimizer with an initial learning rate of 5e-4 and a minimum learning rate of 5e-6 was utilized for training the model. A cosine learning rate scheduler was used to adjust the learning rate during training. Owing to the limited dataset size in this study, transfer learning was applied to fine-tune ACF-Net, where the backbone was initialized with weights pre-trained on the Cityscapes dataset [51]. The model was fine-tuned for 150 epochs with a batch size of 8. For computational efficiency, all images were resized from the original size to  $520 \times 520$  pixels. The model achieving the lowest loss on the validation dataset was saved as the final model.

The ACF-Net was evaluated through comparative studies that measure its performance against related models and state-of-the-art summarized below.

- *Single-task models:* Two models, that use HRNetV2-W48 as the backbone, were trained separately using the hyperparameters mentioned

above. They perform the bridge element parsing and defect segmentation tasks, respectively. The two single-task models serve as the baseline for assessing MTL models in this paper.

- *Variants of ACF-Net*: Three variants of ACF-Net were trained to evaluate the design of ACF-Net. The Naïve MTL model drops both the task-specific relearning (TR) subnets and the co-interactive fusion (CF) module from the ACF-Net. The ACF-Net w/o TR is the model that drops only the task-specific relearning subnets, whereas the ACF-Net w/o CF drops only the co-interactive fusion module.
- *State-of-the-art models*: The recently developed MTL models, including MaDnet [12], MT-HRNet [13], and MTL-I [14], have shown state-of-the-art performance in segmenting both bridge elements and surface defects. ACF-Net was compared to these models to demonstrate the improvement it can achieve. To ensure a fair comparison, these networks were trained and tested on the SBCIV dataset using the same data augmentation methods. The training and testing of these models strictly followed the hyperparameter settings in their papers.

#### 4.3. Evaluation metrics

Comprehensive metrics at the class-level, task-level, and model-level are defined. For any of the datasets, a vector of binary variables,  $\mathbf{y}_{i,j}$ , denotes the ground truth of class  $j$  in task  $i$  for all pixels in that dataset, and the other vector of binary variables,  $\hat{\mathbf{y}}_{i,j}$ , is the prediction.  $\Lambda_i$  designates the set of classes in task  $i$ , for  $i \in \{e, d\}$ . Here,  $\Lambda_e = \{\text{Bearing, Bracing, Deck, Floor beam, Girder, Substructure, Background}\}$  is the set of classes in the bridge element parsing task, and  $\Lambda_d = \{\text{Corrosion, Non-corrosion}\}$  is the set of classes in the defect segmentation task. In performing task  $i$ , a model's ability to predict class  $j$  pixels is assessed using three widely recognized metrics, namely Intersection over Union (IoU), Precision, and Recall:

$$\text{IoU}_{i,j} = \frac{\|\mathbf{y}_{i,j} \wedge \hat{\mathbf{y}}_{i,j}\|_1}{\|\mathbf{y}_{i,j} \vee \hat{\mathbf{y}}_{i,j}\|_1} \quad (9)$$

$$\text{Precision}_{i,j} = \frac{\|\mathbf{y}_{i,j} \wedge \hat{\mathbf{y}}_{i,j}\|_1}{\|\hat{\mathbf{y}}_{i,j}\|_1} \quad (10)$$

$$\text{Recall}_{i,j} = \frac{\|\mathbf{y}_{i,j} \wedge \hat{\mathbf{y}}_{i,j}\|_1}{\|\mathbf{y}_{i,j}\|_1} \quad (11)$$

where  $\wedge$  is the element-wise AND operator,  $\vee$  is the element-wise OR operator, and  $\|\cdot\|_1$  is norm 1 that can count the non-zero elements of the vector.  $\text{IoU}_{i,j}$  in Eq. (9) calculates the intersection of the class  $j$  ground truth and the prediction over their union, for any  $j \in \Lambda_i$ .  $\text{Precision}_{i,j}$  in Eq. (10) is the percentage of pixels predicted as class  $j$  which are predicted correctly, and  $\text{Recall}_{i,j}$  in Eq. (11) is the percentage of class  $j$  pixels that are correctly predicted.

For the task-level evaluation, three commonly used metrics were adopted, which are mean IoU (mIoU), mean Accuracy (mAcc), and pixel Accuracy (pAcc). For any task  $i$ , mIoU is calculated by averaging the IoU values of all the classes. mAcc is the mean of class-level accuracy values, whereas pAcc denotes the accuracy evaluated at the pixel-level without regard to the classes.

$$\text{mIoU}_i = \frac{1}{|\Lambda_i|} \sum_{j \in \Lambda_i} \text{IoU}_{i,j} \quad (12)$$

$$\text{mAcc}_i = \frac{1}{|\Lambda_i|} \sum_{j \in \Lambda_i} \frac{\|\mathbf{y}_{i,j} \wedge \hat{\mathbf{y}}_{i,j}\|_1}{\|\mathbf{y}_{i,j}\|_1} \quad (13)$$

$$\text{pAcc}_i = \frac{\sum_{j \in \Lambda_i} \|\mathbf{y}_{i,j} \wedge \hat{\mathbf{y}}_{i,j}\|_1}{\sum_{j \in \Lambda_i} \|\mathbf{y}_{i,j}\|_1} \quad (14)$$

Finally, at the model-level, using the two single-task models as the baseline, the study measured the incremental of a MTL model's overall performance against the baseline by averaging the percentage increase of every task-level metric:

$$\Delta = \frac{1}{6} \sum_{i \in \Omega} [\Delta(\text{mIoU}_i) + \Delta(\text{mAcc}_i) + \Delta(\text{pAcc}_i)] \quad (15)$$

where  $\Delta(\cdot)$  means the percentage increase of a metric.

## 5. Experiments and results

Experiments are conducted to verify the effectiveness of the proposed ACF-Net on the newly developed SBCIV dataset.

### 5.1. Ablation study

Ablation study was performed to thoroughly evaluate the effectiveness of the key components designed for ACF-Net. The single-task models utilizing the HRNetV2-W48, along with variants of the ACF-Net, were trained and pitted against the ACF-Net. Results are summarized in Table 1 and discussed below.

Table 1: Ablation study.

Method	Element Parsing			Defect Segmentation		
	mIoU	mAcc	pAcc	mIoU	mAcc	pAcc
Single-task	91.86	95.34	96.96	84.88	90.34	96.91
Naïve MTL	89.60	94.86	96.61	85.26	90.54	97.07
ACF-Net w/o CF	91.83	95.25	96.40	85.61	90.00	97.20
ACF-Net w/o TF	91.62	95.16	97.23	86.72	90.63	97.42
ACF-Net	<b>92.11</b>	<b>95.56</b>	<b>97.27</b>	<b>87.16</b>	<b>90.79</b>	<b>97.54</b>

*Note:* The highest value for each performance metric among all networks is in bold.

w/o = without; CF = co-interactive fusion module; TF = task-specific feature relearning subnets.

From Table 1, it can be observed that the naïve MTL model is dominated by the defect segmentation task, as compared to the single-task models. Although the IoU value of defect segmentation has slightly improved by 0.38%, the IoU value of element parsing has significantly dropped by 2.26%. Therefore, the naïve MTL model exhibits an overall decline in performance compared to the single-task models. It indicates that performing two different tasks by directly utilizing the overall feature embedding from the shared deep feature extractor is not as effective as the task-specific single-task models.

After introducing the two task-specific feature relearning subnets, the naïve MTL model becomes the ACF-Net w/o CF model in Table 1. The added subnets in the ACF-Net w/o CF model effectively enhance the performance, resulting in a respective improvement of 2.23% and 0.35% in the IoU values of the two tasks, as compared to the naïve MTL model. The observed improvement justifies the effectiveness of further-learned task-specific features from the overall deep feature for the downstream tasks.

The ACF-Net w/o TF is obtained by adding the co-interactive fusion module to the naïve MTL model. Compared to the single-task models, the ACF-Net w/o TF maintains equivalent performance levels on the task of element parsing yet displays a significant improvement in the task of defect segmentation. The comparison demonstrates the benefit of incorporating spatial information of structural elements in the defect segmentation task, and vice versa.

Different from the naïve MTL model, the proposed ACF-Net has both the task-specific relearning subnets and the co-interactive fusion module. ACF-Net effectively addresses the limitation of the naïve MTL model, evidenced by increases of the task-level metrics for 0.25~2.51%. ACF-Net has exceeded the performance of the two single-task models on all metrics for 0.22~2.28%.

## 5.2. Comparison to state-of-the-art models

### 5.2.1. Quantitative comparisons

**Comparison at the task-level.** This study compared the proposed ACF-Net with existing models: MaDnet [12], MT-HRNet [13], and MTL-I [14]. The following discussion is mainly based on mIoU values. Observations from the model comparisons using other metrics, such as mAcc and pAcc, are similar.

Table 2 shows that MaDnet, using a small single-scale hand-designed network, achieves 74.85% and 78.66% mIoU on the element parsing task and defect segmentation task, respectively. MT-HRNet, which uses the most lightweight HRNetV2-W18 as the feature extractor, performs slightly better on the two tasks. However, among all the models considered, MaDnet and MT-HRNet exhibit the least favorable performance, which could be attributed to the utilization of less powerful encoders. Naïve MTL model effectively boosts the two tasks' mIoU values to 89.60% and 85.26% by utilizing the most robust version of HRNet, HRNetV2-W48, as the encoder, although it keeps the same architecture as MT-HRNet. In comparison to the naïve MTL model, MTL-I maintains comparable results on the two tasks, despite utilizing a moderately powerful encoder, HRNetV2-W36. This can be attributed to the well-designed feature projection module and the efficient cross-talk feature sharing between the two tasks. Among all the compared methods, ACF-Net achieves the best performance in all the metrics, whose mIoU values are 17.26% and 8.50% higher than MaDnet's values, further verifying the advantage of the proposed approach.

Table 2: Quantitative comparison results with the state-of-the-art methods on task-level.

Method	Element Parsing			Defect Segmentation		
	mIoU	mAcc	pAcc	mIoU	mAcc	pAcc
MaDnet [12]	74.85	83.54	90.66	78.66	84.58	95.67
MT-HRNet [13]	78.09	87.88	91.56	79.76	85.39	95.93
Naive MTL	89.60	94.86	96.61	85.26	90.54	97.07
MTL-I [14]	89.07	94.54	96.17	84.30	90.07	96.84
<b>ACF-Net (Ours)</b>	<b>92.11</b>	<b>95.56</b>	<b>97.27</b>	<b>87.16</b>	<b>90.79</b>	<b>97.54</b>

*Note:* The highest value for each performance metric among all networks is in bold.

**Comparison at the class-level.** ACF-Net also achieves good performance at the class-level compared to state-of-the-art models, as shown in Table 3. ACF-Net clearly outperforms the competitors among all classes. MaDnet and MT-HRNet are notably less capable of segmenting bracings and floor beams than other types of elements, which could be attributed to their irregular shapes. For example, bracings are predominantly cross-shaped. Compared to MaDnet, the naïve MTL model increases the IoU values in segmenting bracings for 27.56% and 11.23% for segmenting floor beams. The significant improvement is merely due to upgrading the encoder to a more capable one. Compared to the naïve MTL model, the MTL-I model further increases the IoU in segmenting bracings for another 0.18% and 6.29% in segmenting floor beams, indicating the effectiveness of feature disentanglement and information sharing through the co-interactive feature fusion in segmenting irregularly shaped elements. Ultimately, ACF-Net achieves the highest IoUs, 92.11% in segmenting bracings and 86.19% in segmenting floor beams. The increased IoUs for another 5.30% and 0.37% that ACF-Net achieved, compared to MTL-I, indicate that the relearning subnets and the co-interactive fusion module are better designs than their counterparts in MTL-I. In segmenting girders and substructures, which represent the majority of pixels across all classes, all models demonstrate at least acceptable results. A noticeable trend is observed, where the IoU value progressively increases from the leftmost to the rightmost model. The progress improvements are mainly due to the introduction of a powerful deep feature extractor, feature disentanglement or relearning, and feature fusion to MTL. The increases

Table 3: Class-level comparison results with the state-of-the-art methods on IoU metric.

Class \ Method	MaD-net [12]	MT-HRNet [13]	Naïve MTL	MTL -I [14]	<b>ACF-Net (Ours)</b>
Element					
Bearing	72.69	74.76	90.47	88.32	<b>91.68</b>
Bracing	59.07	66.00	86.63	86.81	<b>92.11</b>
Deck	79.81	87.76	92.77	90.99	<b>94.89</b>
Floor beam	68.30	67.56	79.53	85.82	<b>86.19</b>
Girder	88.81	88.76	95.61	95.65	<b>96.68</b>
Substructure	87.91	89.39	96.02	94.35	<b>96.16</b>
Background	67.38	72.49	86.21	81.58	<b>87.09</b>
Defect					
No Corrosion	95.34	95.61	96.80	96.56	<b>97.32</b>
Corrosion	61.97	63.90	73.71	72.05	<b>76.99</b>

*Note:* The highest values of each metric for each class among all networks are shown in bold.

in IoU values in segmenting bearings and decks are primarily attributed to using HRNet as the deep feature extractor.

ACF-Net also demonstrates dominantly better performance in segmenting defects than other models. Compared to MaDnet, ACF-Net increases the IoU value in segmenting corrosion by 15.02%, with 11.74% contributed by the adoption of HRNetV2-W48 as the backbone and the remaining 3.28% from feature relearning and co-interactive feature fusion. ACF-Net also increases the ability to segment non-corrosion areas by 1.98%.

### 5.2.2. Qualitative comparison

Fig. 6 illustrates five examples of bridge element parsing and defect segmentation results to demonstrate the effectiveness of the proposed ACF-Net. These examples represent various scenarios with extensive, partial, and scarcely defects.

The qualitative evaluation of the element parsing results demonstrates that ACF-Net generates superior predictions, as evidenced by the segmentation of small objects, such as the distant floor beam in Fig. 6(b), bearings in Fig. 6(c), distant small bracing in Fig. 6(d), and floor beam in Fig. 6(e). This is also apparent in segmenting irregular elements, as demonstrated by the

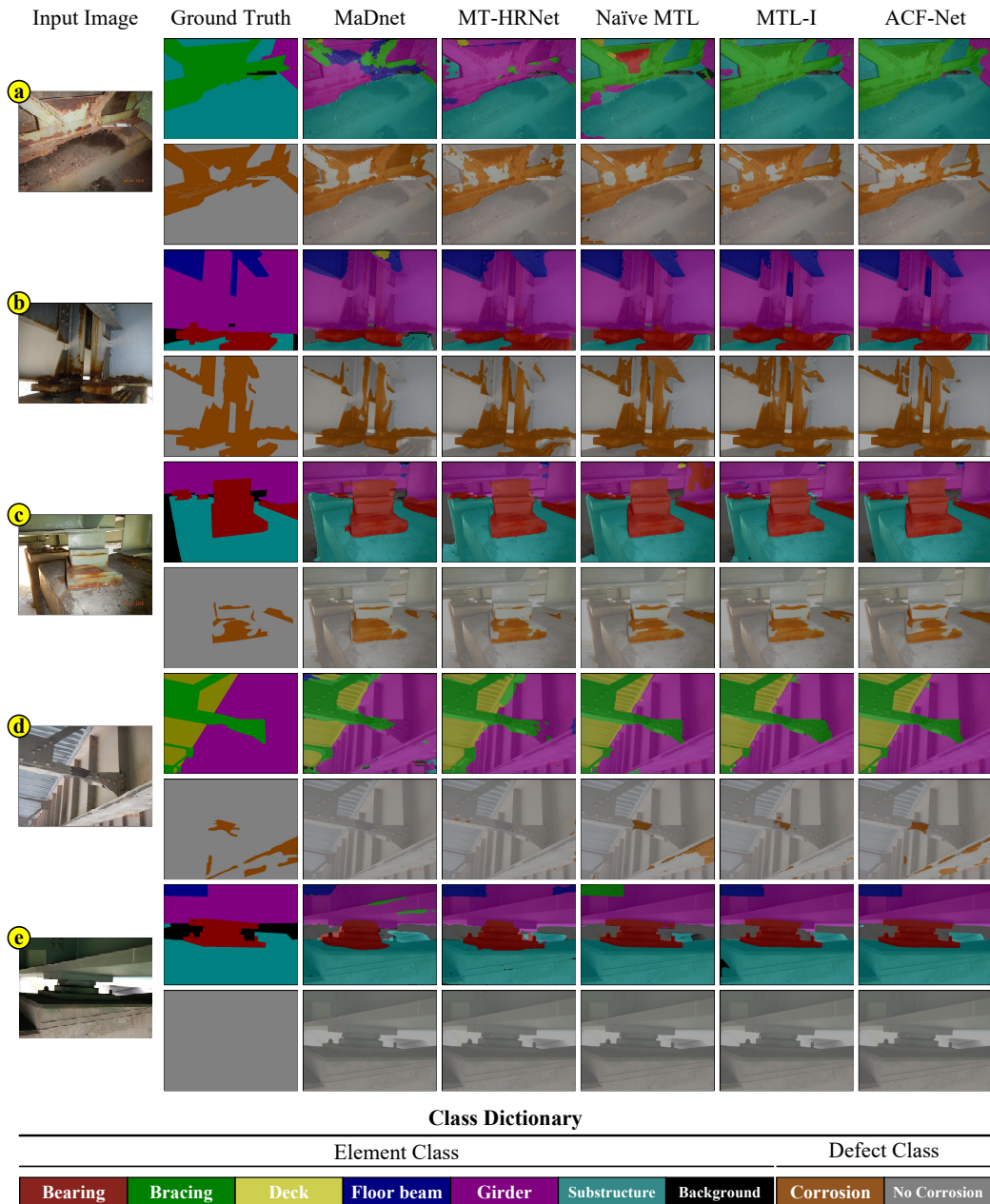


Figure 6: Qualitative comparison with the state-of-the-art.

bracings in Fig. 6(a)(d). Furthermore, ACF-Net facilitates more pronounced and smooth edges of object segmentation, as evidenced by the boundary segmentation of the floor beam in Fig. 6(b) and substructure in Fig. 6(e).

The qualitative comparison of the defect segmentation results reveals that ACF-Net can produce competitive outcomes, as it generates fewer false positives than other methods when the corrosion area is small or less visible, which is evident in Fig. 6(b)(c)(d).

Figure 7 further presents ACF-Net’s results in analyzing fourteen examples from the testing dataset. It is evident that the predictions given by ACF-Net exhibit high quality and closely align with the ground truth.

### 5.2.3. Model complexity comparison

A deep learning model’s complexity, measured by the number of parameters, could be a cost of the model’s performance improvement. Therefore, the performance assessment should keep the model complexity in consideration. Figure 8 presents ACF-Net and other state-of-the-art models on the diagram of performance increment  $\Delta$  at the model-level vs. model complexity (parameters in millions). MaDnet has the fewest parameters due to its simplistic structure, while MT-HRNet has slightly more parameters because it utilizes the lightweight HRNetV2-W18. Consequently, the performance of these two models is less than ideal. MTL-I, which employs HRNetV2-W32 as its backbone, results in a significant performance improvement compared to MaDnet and MT-HRNet. The performance of MTL-I still falls below the single-task baseline, but its parameters are about 77% less than the baseline. By replacing the backbone of MTL-I with HRNetV2-W48, the upgraded version, MTL-I (W48), outperforms its HRNetV2-W36 counterpart and the single-task models. When MT-HRNet’s backbone is changed to HRNetV2-W48, the newer version, MT-HRNet (HRNetV2-W48), and naïve MTL share the same architecture and the number of parameters, yet naïve MTL performs substantially better due to the optimized selection of hyper-parameters. ACF-Net achieves the best performance among all models, with approximately half of the parameters of the single-task models. Compared to MaDnet, ACF-Net’s complexity is increased by 72.96 million, with the majority (62.11 million) added by adopting the HRNetV2-W48 as the backbone for representation learning and the remainder (10.85 million) from the relearning subnets and co-interactive fusion module.

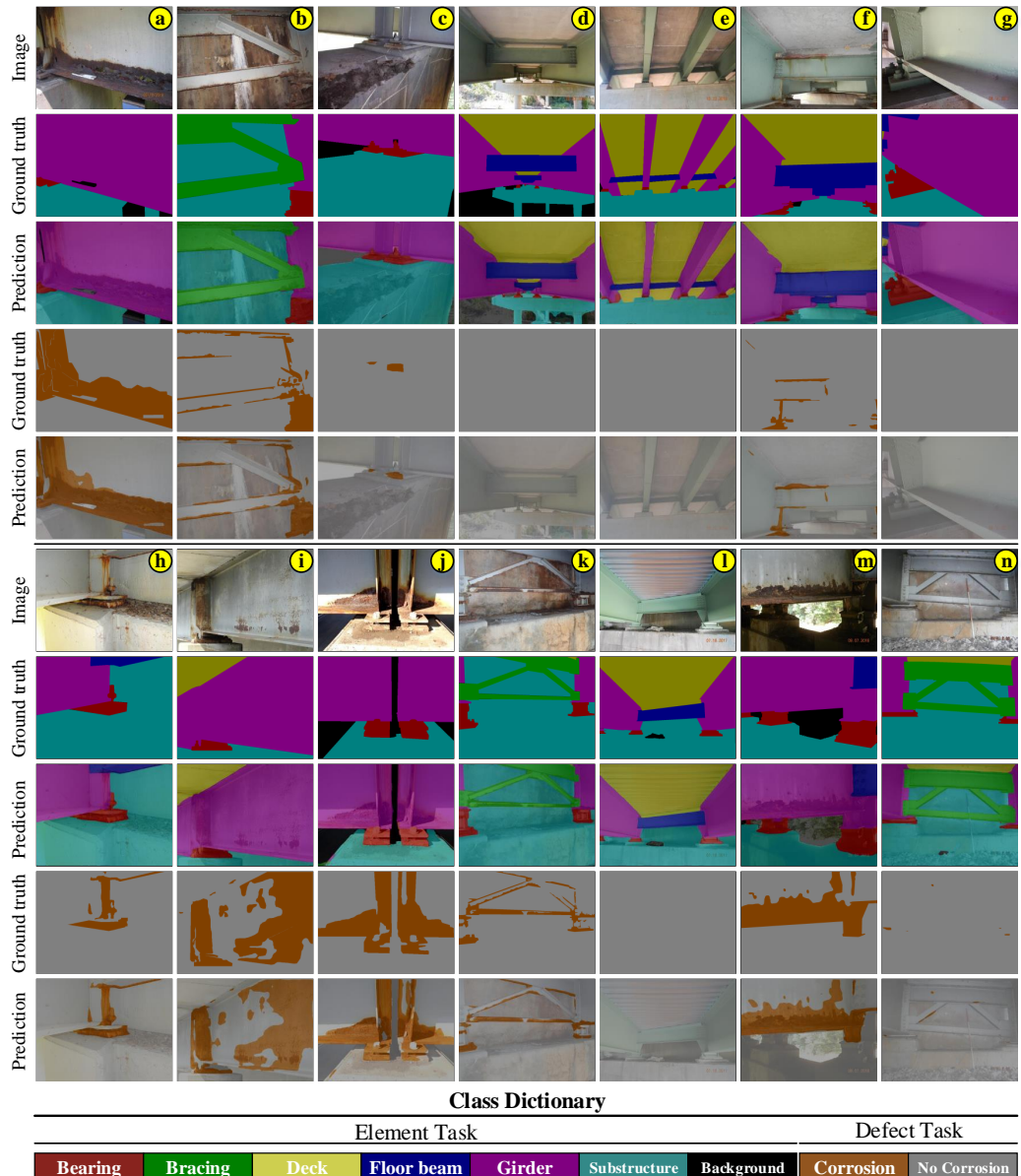


Figure 7: Examples of ACF-Net on the testing dataset.

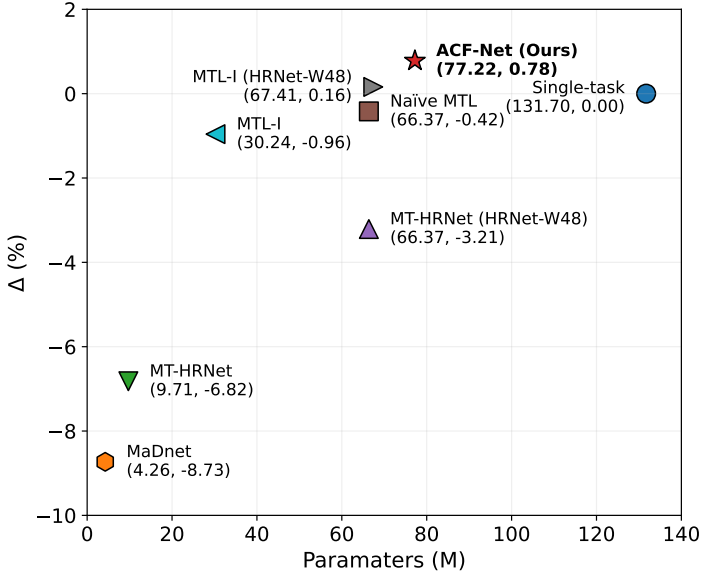


Figure 8: Comparison of parameters and performance evaluation.

### 5.3. Understanding of feature maps and masks

Task-specific feature relearning and co-interactive feature fusion are two important designs for ACF-Net. To better comprehend the roles of those modules, feature maps ( $\mathbf{f}$ ,  $\mathbf{f}_e$ ,  $\mathbf{f}_d$ ,  $\mathbf{f}_e^*$ ,  $\mathbf{f}_d^*$ ) and attention masks ( $\mathbf{S}_e$  and  $\mathbf{S}_d$ ) learned by ACF-Net are visualized in Fig. 9. These visualizations utilize the feature embeddings from the second channel to show primary features, with the values of each image rescaled to be within the range from 0 to 255 to accommodate the colors. Bicubic interpolation is applied to resize the feature maps and attention masks to  $520 \times 520$ , the dimension of the input images of ACF-Net.

The 2nd row in Fig. 9 visualizes the overall feature embedding  $\mathbf{f}$  that essentially encompasses information relevant to both tasks. With the two feature relearning subnets, the element-specific feature map  $\mathbf{f}_e$  and defect-specific feature map  $\mathbf{f}_d$  are respectively extracted from the overall feature embedding. The 3rd row visualizes the element-specific feature map that primarily captures relatively global information about elements, such as position, shape, and scale. In contrast, the defect-specific feature map visualized

in the 4th row mainly captures appearance information of surface defects, such as texture and color. The 5th row visualizes the element mask  $S_e$ , whereas the 6th row presents the defect mask  $S_d$ . A distinct difference in the two tasks' attention masks is evident. Each task's mask functions as a feature selector that masks out uninformative portions of the other task's feature map in feature fusion. It is noteworthy that the element masks exhibit a significantly higher contrast, transitioning from blue to yellow, while the defect masks predominantly present a yellow hue in the same area. This finding implies that the element task benefits more from the extraction of task-specific features. The 7th and 8th rows are spatial-attention-enhanced feature maps  $f_e^*$  and  $f_d^*$ . Compared to  $f_e$  in the 3rd row,  $f_e^*$  in the 7th row captures more detailed appearance information about the elements and thus enhances the ability to differentiate different types of elements. Similarly, compared to  $f_d$  (the 4th row),  $f_d^*$  (the 8th row) integrates the context information about where the defect is developed, which enhances the ability to differentiate defects from defect-like texture such as watermarks on substructures and shadows.

## 6. Case study on structural condition assessment

The potential application of the ACF-Net in bridge inspection is further illustrated in a preliminary structural condition assessment case study. To illustrate how ACF-Net performs the visual assessment for bridge elements, ten examples in the testing dataset are presented in Fig. 10. Each steel element is preliminarily evaluated based on the proportion of the corroded area observed on the element (the ratio of the corroded area to the entire element area). The structural conditions of bridge elements are then categorized into four distinct levels: Good, Fair, Poor, and Severe. These classifications are determined by specific thresholds of corrosion coverage: 0%, 25%, and 50%. These thresholds, which define the intervals between the various condition classifications, are graphically depicted in Fig. 2.

ACF-Net demonstrates promising initial evaluation results in scenarios where the bridge elements are in good condition, as illustrated in Fig. 10(c)(g). Moreover, the proposed method is capable of accurately identifying the elements of interest in cases with severe damage, even when there is extensive surface deterioration. The ACF-Net provides precise preliminary evaluation outcomes in such instances, as displayed in Fig. 10(a)(d)(e)(f)(j). In scenes featuring a mixture of elements in both well or unsatisfactory conditions,

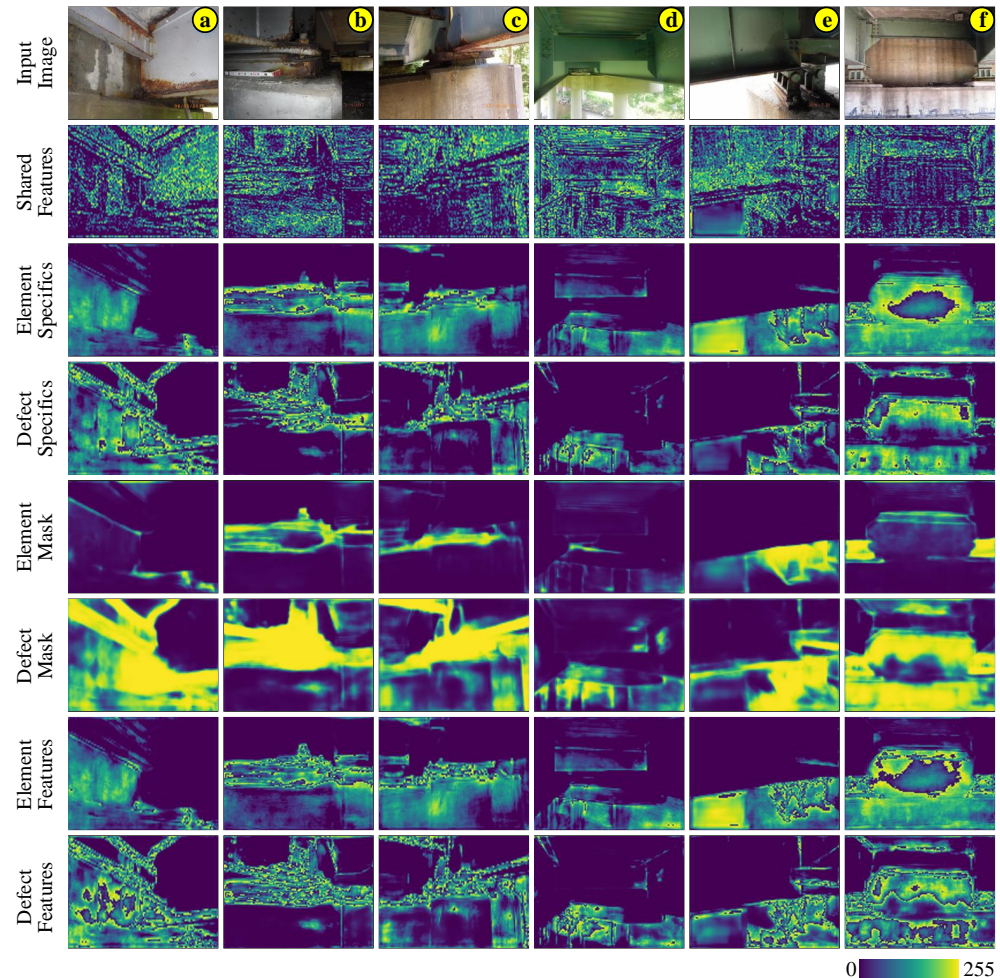


Figure 9: Visualization of image feature evolution and attention masks.

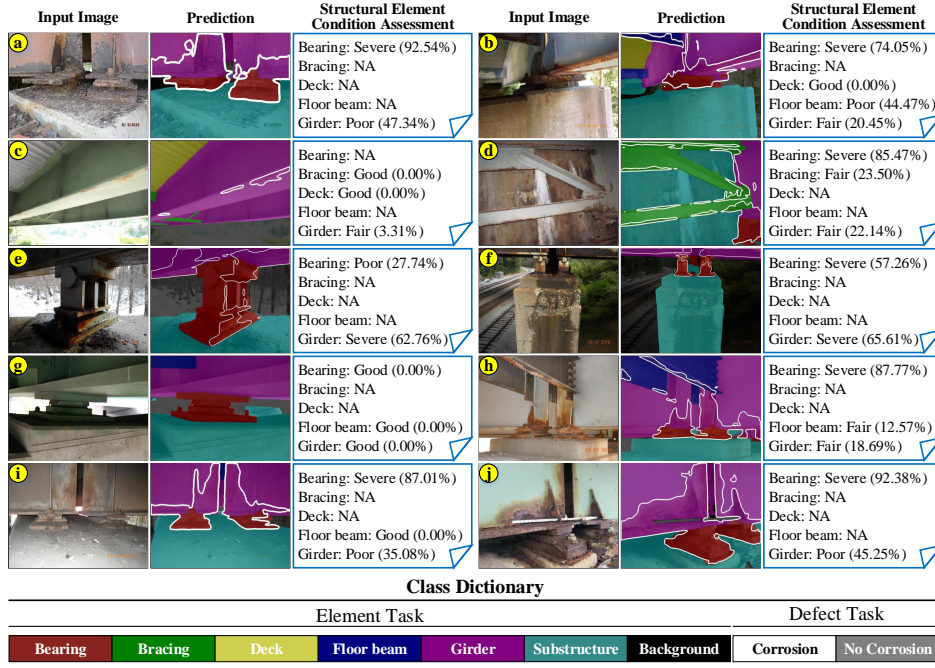


Figure 10: Structural condition assessment examples.

ACF-Net is capable of accurately determining the condition of each element, which can be observed in Fig. 10(b)(h)(i). This level of accuracy and reliability in detecting and assessing both well-maintained and heavily damaged bridge elements underscores the potential of ACF-Net as a valuable tool in the field of infrastructure inspection.

## 7. Conclusions

This paper presented a novel deep learning architecture called Attention-enhanced Co-interactive Fusion Network (ACF-Net), and a newly annotated Steel Bridge Condition Inspection Visual (SBCIV) dataset, to automate visual bridge inspection for structural condition assessment. ACF-Net employs a share-split-interaction pipeline, with the shared component utilizing a deep, high-resolution encoder HRNetV2-W48. The split-interaction component comprises two task-specific relearning subnets and one co-interactive feature fusion module. ACF-Net has surpassed the current state-of-the-art MTL methods for structural condition assessment, achieving 92.11% element parsing mIoU and 87.16% corrosion segmentation mIoU on the testing

dataset of SBCIV. The ablation study revealed how ACF-Net’s key modules contribute to performance improvement, and the evaluation on the testing dataset further demonstrated the capability of ACF-Net in automated visual inspection.

While ACF-Net has shown promising results in extracting structural elements in inspection images and assessing the elements’ condition, addressing limitations presented in the current work will broaden the impact of ACF-Net on the visual inspection of civil infrastructure. One obstacle to be addressed is the scarcity of annotated data. Bridges are diverse in types and designs. The condition of the same bridge is also changing over time due to deterioration or reparation. The performance of ACF-Net will drop by a certain amount if the inspection images contain new elements and new defect types. Annotated data are required to adapt ACF-Net to new tasks. An efficient data annotation tool is desired to accommodate the need for annotated data. A portion of the improved task performance achieved by ACF-Net is attributed to the use of a deep feature encoder. Deep feature extraction is the most time-consuming portion of image analysis. Lightweight feature extractors that are as powerful as the deep feature extractors are desired because the runtime efficiency would support inspectors’ decisions at inspection fields, such as utilizing additional advanced inspection methods (e.g., infrared cameras, ground-penetrating radar, ultrasound scanning) to collect data at concerned areas identified from the visual inspection. Those future works will move the research on this topic forward, and the automation of infrastructure inspection will continue blooming.

## 8. Acknowledgement

This work was supported by the National Science Foundation (grant numbers ECCS-2025929, ECCS-2026357). Any opinions, findings, conclusions, or recommendations expressed in this material are those of the authors and do not necessarily reflect the views of the National Science Foundation.

## References

- [1] B. A. Graybeal, B. M. Phares, D. D. Rolander, M. Moore, G. Washer, Visual inspection of highway bridges, *Journal of Nondestructive Evaluation* 21 (2002) 67–83.

- [2] I.-H. Kim, S. Yoon, J. H. Lee, S. Jung, S. Cho, H.-J. Jung, A comparative study of bridge inspection and condition assessment between manpower and a uas, *Drones* 6 (2022).
- [3] F. Outay, H. A. Mengash, M. Adnan, Applications of unmanned aerial vehicle (uav) in road safety, traffic and highway infrastructure management: Recent advances and challenges, *Transportation Research Part A: Policy and Practice* 141 (2020) 116–129. doi:<https://doi.org/10.1016/j.tra.2020.09.018>.
- [4] B. F. Spencer Jr, V. Hoskere, Y. Narazaki, Advances in computer vision-based civil infrastructure inspection and monitoring, *Engineering* 5 (2019) 199–222.
- [5] Federal Highway Administration (FHWA), National bridge inspection standards, 2022.
- [6] American Association of State Highway and Transportation Officials (AASHTO), Manual for bridge element inspection, 2nd edition, 2019.
- [7] T. W. Ryan, C. E. Lloyd, M. S. Pichura, D. M. Tarasovich, S. Fitzgerald, Bridge inspector's reference manual (BIRM), Technical Report, United States. Federal Highway Administration, 2022.
- [8] A. E2018-15, Standard guide for property condition assessments: baseline property condition assessment process, 2015.
- [9] Y. Narazaki, V. Hoskere, T. A. Hoang, Y. Fujino, A. Sakurai, B. F. Spencer Jr., Vision-based automated bridge component recognition with high-level scene consistency, *Computer-Aided Civil and Infrastructure Engineering* 35 (2020) 465–482. doi:<https://doi.org/10.1111/mice.12505>.
- [10] M. M. Karim, R. Qin, G. Chen, Z. Yin, A semi-supervised self-training method to develop assistive intelligence for segmenting multiclass bridge elements from inspection videos, *Structural Health Monitoring* 21 (2022) 835–852.
- [11] E. Bianchi, M. Hebdon, Visual structural inspection datasets, *Automation in Construction* 139 (2022) 104299. doi:<https://doi.org/10.1016/j.autcon.2022.104299>.

- [12] V. Hoskere, Y. Narazaki, T. A. Hoang, B. Spencer Jr, Madnet: Multi-task semantic segmentation of multiple types of structural materials and damage in images of civil infrastructure, *Journal of Civil Structural Health Monitoring* 10 (2020) 757–773.
- [13] X.-W. Ye, S.-Y. Ma, Z.-X. Liu, Y. Ding, Z.-X. Li, T. Jin, Post-earthquake damage recognition and condition assessment of bridges using uav integrated with deep learning approach, *Structural Control and Health Monitoring* 29 (2022) e3128. doi:<https://doi.org/10.1002/stc.3128>.
- [14] C. Zhang, M. M. Karim, R. Qin, A multitask deep learning model for parsing bridge elements and segmenting defect in bridge inspection images, *Transportation Research Record* (2023) 03611981231155418. doi:<https://doi.org/10.1177/03611981231155418>.
- [15] Y. Zhang, Q. Yang, A survey on multi-task learning, *IEEE Transactions on Knowledge and Data Engineering* 34 (2021) 5586–5609.
- [16] E. Bianchi, A. L. Abbott, P. Tokek, M. Hebdon, Coco-bridge: Structural detail data set for bridge inspections, *Journal of Computing in Civil Engineering* 35 (2021) 04021003.
- [17] G. Yang, K. Liu, J. Zhang, B. Zhao, Z. Zhao, X. Chen, B. M. Chen, Datasets and processing methods for boosting visual inspection of civil infrastructure: A comprehensive review and algorithm comparison for crack classification, segmentation, and detection, *Construction and Building Materials* 356 (2022) 129226. doi:<https://doi.org/10.1016/j.conbuildmat.2022.129226>.
- [18] W. Hu, W. Wang, C. Ai, J. Wang, W. Wang, X. Meng, J. Liu, H. Tao, S. Qiu, Machine vision-based surface crack analysis for transportation infrastructure, *Automation in Construction* 132 (2021) 103973. doi:<https://doi.org/10.1016/j.autcon.2021.103973>.
- [19] S. Zhou, C. Canchila, W. Song, Deep learning-based crack segmentation for civil infrastructure: data types, architectures, and benchmarked performance, *Automation in Construction* 146 (2023) 104678. doi:<https://doi.org/10.1016/j.autcon.2022.104678>.

- [20] A. Khan, A. Sohail, U. Zahoor, A. S. Qureshi, A survey of the recent architectures of deep convolutional neural networks, *Artificial Intelligence Review* 53 (2020) 5455–5516.
- [21] R. Ali, J. H. Chuah, M. S. A. Talip, N. Mokhtar, M. A. Shoaib, Structural crack detection using deep convolutional neural networks, *Automation in Construction* 133 (2022) 103989. doi:<https://doi.org/10.1016/j.autcon.2021.103989>.
- [22] C. V. Dung, L. D. Anh, Autonomous concrete crack detection using deep fully convolutional neural network, *Automation in Construction* 99 (2019) 52–58. doi:<https://doi.org/10.1016/j.autcon.2018.11.028>.
- [23] J. Long, E. Shelhamer, T. Darrell, Fully convolutional networks for semantic segmentation, in: *Proceedings of the IEEE conference on computer vision and pattern recognition*, 2015, pp. 3431–3440.
- [24] A. Ji, X. Xue, Y. Wang, X. Luo, W. Xue, An integrated approach to automatic pixel-level crack detection and quantification of asphalt pavement, *Automation in Construction* 114 (2020) 103176. doi:<https://doi.org/10.1016/j.autcon.2020.103176>.
- [25] L.-C. Chen, Y. Zhu, G. Papandreou, F. Schroff, H. Adam, Encoder-decoder with atrous separable convolution for semantic image segmentation, in: *Proceedings of the European Conference on Computer Vision (ECCV)*, 2018, pp. 801–818.
- [26] Q. Mei, M. Gü, M. R. Azim, Densely connected deep neural network considering connectivity of pixels for automatic crack detection, *Automation in Construction* 110 (2020) 103018. doi:<https://doi.org/10.1016/j.autcon.2019.103018>.
- [27] F. Liu, L. Wang, Unet-based model for crack detection integrating visual explanations, *Construction and Building Materials* 322 (2022) 126265. doi:<https://doi.org/10.1016/j.conbuildmat.2021.126265>.
- [28] O. Ronneberger, P. Fischer, T. Brox, U-net: Convolutional networks for biomedical image segmentation, in: *Medical Image Computing and Computer-Assisted Intervention–MICCAI 2015: 18th International Conference, Munich, Germany, October 5–9, 2015, Proceedings, Part III* 18, Springer, 2015, pp. 234–241.

- [29] D. J. Atha, M. R. Jahanshahi, Evaluation of deep learning approaches based on convolutional neural networks for corrosion detection, *Structural Health Monitoring* 17 (2018) 1110–1128. doi:<https://doi.org/10.1177/1475921717737051>.
- [30] A. Rahman, Z. Y. Wu, R. Kalfarisi, Semantic deep learning integrated with rgb feature-based rule optimization for facility surface corrosion detection and evaluation, *Journal of Computing in Civil Engineering* 35 (2021) 04021018.
- [31] L.-C. Chen, G. Papandreou, I. Kokkinos, K. Murphy, A. L. Yuille, Deeplab: Semantic image segmentation with deep convolutional nets, atrous convolution, and fully connected crfs, *IEEE Transactions on Pattern Analysis and Machine Intelligence* 40 (2018) 834–848. doi:<https://doi.org/10.1109/TPAMI.2017.2699184>.
- [32] Q. Han, N. Zhao, J. Xu, Recognition and location of steel structure surface corrosion based on unmanned aerial vehicle images, *Journal of Civil Structural Health Monitoring* 11 (2021) 1375–1392.
- [33] T.-Y. Lin, P. Dollár, R. Girshick, K. He, B. Hariharan, S. Belongie, Feature pyramid networks for object detection, in: *Proceedings of the IEEE Conference on Computer Vision and Pattern Recognition*, 2017, pp. 2117–2125.
- [34] S. Liu, L. Qi, H. Qin, J. Shi, J. Jia, Path aggregation network for instance segmentation, in: *Proceedings of the IEEE Conference on Computer Vision and Pattern Recognition*, 2018, pp. 8759–8768.
- [35] F. Jiang, Y. Ding, Y. Song, F. Geng, Z. Wang, Automatic pixel-level detection and measurement of corrosion-related damages in dim steel box girders using fusion-attention-u-net, *Journal of Civil Structural Health Monitoring* 13 (2023) 199–217.
- [36] I. Katsamenis, N. Doulamis, A. Doulamis, E. Protopapadakis, A. Voulodimos, Simultaneous precise localization and classification of metal rust defects for robotic-driven maintenance and prefabrication using residual attention u-net, *Automation in Construction* 137 (2022) 104182. doi:<https://doi.org/10.1016/j.autcon.2022.104182>.

- [37] Y. Gao, K. M. Mosalam, Deep transfer learning for image-based structural damage recognition, *Computer-Aided Civil and Infrastructure Engineering* 33 (2018) 748–768. doi:<https://doi.org/10.1111/mice.12363>.
- [38] C. M. Yeum, J. Choi, S. J. Dyke, Automated region-of-interest localization and classification for vision-based visual assessment of civil infrastructure, *Structural Health Monitoring* 18 (2019) 675–689. doi:<https://doi.org/10.1177/1475921718765419>.
- [39] T. Czerniawski, F. Leite, Automated segmentation of rgb-d images into a comprehensive set of building components using deep learning, *Advanced Engineering Informatics* 45 (2020) 101131. doi:<https://doi.org/10.1016/j.aei.2020.101131>.
- [40] Y. Wang, X. Jing, W. Chen, H. Li, Y. Xu, Q. Zhang, Geometry-informed deep learning-based structural component segmentation of post-earthquake buildings, *Mechanical Systems and Signal Processing* 188 (2023) 110028. doi:<https://doi.org/10.1016/j.ymssp.2022.110028>.
- [41] K. He, G. Gkioxari, P. Dollár, R. Girshick, Mask r-cnn, in: *Proceedings of the IEEE International Conference on Computer Vision*, 2017, pp. 2961–2969.
- [42] C. Zhang, M. M. Karim, Z. Yin, R. Qin, A deep neural network for multiclass bridge element parsing in inspection image analysis, in: *Proceedings of the 8th World Conference on Structural Control and Monitoring (8WCSCM)*, Orlando, Florida, U.S.A, June 5-8, 2022, pp. 1–8.
- [43] J. Wang, K. Sun, T. Cheng, B. Jiang, C. Deng, Y. Zhao, D. Liu, Y. Mu, M. Tan, X. Wang, et al., Deep high-resolution representation learning for visual recognition, *IEEE Transactions on Pattern Analysis and Machine Intelligence* 43 (2020) 3349–3364.
- [44] H.-P. Wan, Y.-Q. Ni, Bayesian multi-task learning methodology for reconstruction of structural health monitoring data, *Structural Health Monitoring* 18 (2019) 1282–1309. doi:<https://doi.org/10.1177/1475921718794953>.

- [45] J. Liu, S. Xu, M. Bergés, H. Y. Noh, Hiermud: Hierarchical multi-task unsupervised domain adaptation between bridges for drive-by damage diagnosis, *Structural Health Monitoring* 22 (2023) 1941–1968. doi:<https://doi.org/10.1177/14759217221081159>.
- [46] S. Sun, X. Wang, J. Li, C. Lian, Landslide evolution state prediction and down-level control based on multi-task learning, *Knowledge-Based Systems* 238 (2022) 107884. doi:<https://doi.org/10.1016/j.knosys.2021.107884>.
- [47] S. Vandenhende, S. Georgoulis, W. Van Gansbeke, M. Proesmans, D. Dai, L. Van Gool, Multi-task learning for dense prediction tasks: A survey, *IEEE transactions on pattern analysis and machine intelligence* 44 (2021) 3614–3633.
- [48] S. Liu, E. Johns, A. J. Davison, End-to-end multi-task learning with attention, in: *Proceedings of the IEEE Conference on Computer Vision and Pattern Recognition*, 2019, pp. 1871–1880.
- [49] E. Bianchi, M. Hebdon, Corrosion condition state semantic segmentation dataset, 2021. doi:<https://doi.org/10.7294/16624663.v2>.
- [50] B. C. Russell, A. Torralba, K. P. Murphy, W. T. Freeman, Labelme: a database and web-based tool for image annotation, *International Journal of Computer Vision* 77 (2008) 157–173.
- [51] M. Cordts, M. Omran, S. Ramos, T. Rehfeld, M. Enzweiler, R. Benenson, U. Franke, S. Roth, B. Schiele, The cityscapes dataset for semantic urban scene understanding, in: *Proceedings of the IEEE Conference on Computer Vision and Pattern Recognition*, 2016, pp. 3213–3223.